IOP Publishing Biofabrication 18 (2026) 015033 https://doi.org/10.1088/1758-5090/ae3c42

Biofabrication

OPEN ACCESS

RECEIVED
26 September 2025

ACCEPTED FOR PUBLICATION
22 January 2026

PUBLISHED
5 February 2026

PAPER

Scaffold-free assembly of cortical–hippocampal circuit from modular neurospheroids: a high-throughput platform to investigate network development and dynamics

Ilaria Donati della Lunga[1], **Francesca Callegari**[1], **Fabio Poggio**[1], **Letizia Cerutti**[1,2], **Mattia Pesce**[2], **Giovanni Lo Bello**[1], **Alessandro Simi**[3], **Mariateresa Tedesco**[1], **Paolo Massobrio**[1,4] **and Martina Brofiga**[1,2,5,*]

[1] Department of Informatics, Bioengineering, Robotics, Systems Engineering (DIBRIS), University of Genova, Genova, Italy
[2] Neurofacility, Istituto Italiano di Tecnologia (IIT), Genova, Italy
[3] Central RNA Laboratory, Istituto Italiano di Tecnologia (IIT), Genova, Italy
[4] National Institute for Nuclear Physics (INFN), Genova, Italy
[5] ScreenNeuroPharm, Sanremo Italy
[*] Author to whom any correspondence should be addressed.

E-mail: martina.brofiga@unige.it

Keywords: neurospheroids, assembloid-like structures, cortex, hippocampus, calcium imaging, brain rhythms, micro-electrode arrays

Supplementary material for this article is available online

Abstract

Three-dimensional *in vitro* models are critical for recapitulating key aspects of neural network development and interregional interactions. We present a scaffold-free modular system based on primary cortical and hippocampal neurospheroids (NSs), which are subsequently coupled to self-assemble into reproducible assembloid-like structures (ASs). Through a multimodal approach, we characterized their morphological, mechanical, metabolic, and functional properties. NSs displayed progressive growth, viability surpassing 2D cultures, and stiffness approaching physiological brain ranges. Immunostaining verified proper neuronal and astrocytic ratios and confirmed a physiologically relevant GABAergic component. Upon coupling, ASs exhibited robust structural integration while maintaining functional modularity. Calcium imaging enabled the investigation of synchronization patterns at modules' interface, while electrophysiology revealed maturation-dependent and configuration-specific emergence of rhythms, a type of activity typically found *in vivo*. Functional excitation–inhibition balance remained constant throughout development and was pharmacologically modulated successfully. Our platform balances biological relevance and experimental tractability, offering a versatile tool for investigating neural circuit development, network dynamics, and region-specific perturbations in a reproducible and scalable *in vitro* environment.

1. Introduction

In vitro neuronal models have long been a cornerstone of biomedical research, providing insights into neuronal dynamics, disease mechanisms, and drug screening [1]. Traditionally, these models have been two-dimensional (2D), with cells cultivated on flat substrates. Although 2D systems are widely used, they fall short in replicating the dynamic microenvironment of native tissues that depends on their complex three-dimensional (3D) architecture [1–3]. This limitation is relevant specifically in the study of the brain, as neurons in 2D often form abnormal connections and exhibit altered behaviours that do not accurately reflect the coordinated and structured activity of the brain [4].

To better mimic the physiological conditions of neural tissues, researchers have adopted 3D *in vitro* models. One of the most significant advances in this area is neurospheroids (NSs), spherical aggregates of neuronal cells that self-organize into structures resembling regions of the brain at early development stages [5–8]. By promoting more natural cell–cell interactions, these 3D assemblies are valuable tools for investigating complex patterns of electrophysiological activity and their computational properties and provide a robust platform for studying key neural processes such as neurogenesis [9], synaptic formation [10], and region-specific signalling [5].

A more elaborate approach is represented by organoids, which are stem cell-derived 3D constructs that undergo partial self-patterning and recapitulate several features of embryonic brain development, including neuroepithelial organization, progenitor zonation, and region-specific differentiation [11]. Building upon these models, assembloids—composite systems resulting from the coupling of organoids—have emerged as groundbreaking platforms that combine multiple brain regions to capture the functional and structural complexity of the brain [12–14]. Assembloids enable the study of interregional communication and dynamic processes such as synaptic connectivity, neural migration, and signal transmission in a physiological-like *in vitro* environment [15]. While assembloids derived from human pluripotent stem cells provide powerful tools for patient-specific modelling, precision medicine applications, and exploring the genetic basis of neurodevelopmental disorders, they also present non-negligible technical and biological challenges. These include batch-to-batch variability, long and expensive differentiation protocols, and often result in heterogeneous tissue composition and size, which limit their reproducibility and scalability [16–18]. Moreover, they typically require embedding in extracellular matrices such as Matrigel, which can influence morphogenesis and complicate downstream structural or functional analysis [19]. These factors make organoid-based assembloids less suitable for applications that demand high throughput, precise timing, or fine control over experimental conditions.

These constraints have led to growing interest in intermediate models that bridge the gap between traditional 2D systems and complex organoid systems.

In this context, we introduced a modular and scaffold-free NS-based model that provides a good compromise between biological relevance and experimental tractability. It allows the generation of assembloid-like structures (ASs) composed of primary heterogeneous (i.e. region-specific) spheroids, offering a controlled environment to investigate interregional interactions, circuit maturation, and emergent network dynamics, while supporting reproducibility, reduced variability, and compatibility with multi-modal analysis.

In particular, we investigated the structural and functional properties of NSs as fundamental building blocks for 3D brain-inspired structures, with a specific focus on studying the cortical–hippocampal interactions. Our setup supported a comprehensive, multi-modal investigation of the circuit, integrating morphological analysis, metabolic and mechanical characterization, calcium imaging, and electrophysiological recordings with Micro-Electrode Arrays (MEAs). Our findings reveal that these models exhibit an overall cellular composition that mostly reflects that of the brain, while guaranteeing effective cell growth and viability. Additionally, the stiffness of NSs falls within the physiological range of brain tissue, driving the formation and maturation of functional networks and ensuring appropriate cellular signalling and tissue integrity. With morphologic analyses, we identified the optimal coupling conditions necessary to achieve robust inter-module interactions. Furthermore, we observed that the 3D configuration of NSs and ASs influenced maturation dynamics, leading to the emergence of distinct activity profiles and synchronization patterns over time. Through calcium imaging and MEA recordings, we proved that neuronal functional interactions evolved as cultures matured and resulted in different brain rhythms whose expression changed throughout development. This suggests that our model effectively captures critical aspects of neurodevelopmental processes, with networks self-organizing differently depending on the source tissue of the NSs and their degree of maturation. Overall, our results emphasize the potential of our 3D model to recapitulate some features of neuronal network organization found *in vivo*, providing a valuable platform for investigating fundamental neurobiological mechanisms and modelling diseases.

2. Materials and methods

2.1. Cell culture preparation

Primary cortical and hippocampal tissues were isolated from rat embryos at gestational day 18 (E18) under sterile conditions. All procedures were carried out to reduce the number of animals and to minimize their suffering. The experimental protocol was approved by the European Animal Care Legislation (2010/63/EU), by the Italian Ministry of Health in accordance with the D.L. 116/1992 and by the guidelines of the University of Genova (Prot-75F11.N.6JI, 08/08/18).

Tissue was dissociated enzymatically with a solution of Hank's Balanced Salt Solution (HBSS) without calcium and magnesium, 0.125% Trypsin, and 0.02 mg ml $^{-1}$ DNase. To guarantee the enzymatic process, the tissue was left in a water bath at 37 °C for 18 min. The process was quenched by replacing the solution with medium (1% Penicillin-Streptomycin, 1% stable L-Glutamine, 2% B-27 supplement, and 96% Neurobasal medium) supplemented with 10% fetal bovine serum. Eventually, mechanical dissociation was carried out with fire-polished Pasteur pipettes. About 8’000 cells were added per well in ultra-low attachment 96-uwells. The low adhesion properties and the shape of the wells induced the creation of a single NS per well. Spheroids were maintained in incubator at 37 °C in a 5% CO_2, 95% humidity atmosphere for 3 weeks by replacing half of the medium every two days. From DIV 6, we switched to BrainPhys neuronal medium supplemented with 2% SM1 supplement, 1% PenStrep, and 1% GlutaMAX [20]. ASs were formed by placing two NSs into the same well of an ultra-low attachment 96-uwells at DIV 9 (unless otherwise specified). This was selected as the optimal coupling day that guarantees the establishment of mutual interaction while maintaining the individual properties of the NSs (figures 3 and S2). Three types of ASs were generated: homogenous cortical–cortical (CC), homogenous hippocampal–hippocampal (HH), and heterogeneous cortical–hippocampal (CH).

2.2. Morphology

The morphological characterization of NSs and ASs was carried out throughout their entire development, from DIV 1 to DIV 14 for NSs and from the day of coupling (DIV 7—DIV 12) to DIV 15 for ASs. Images were acquired using differential interference contrast microscopy with an Olympus IX51 microscope mounting an Olympus SC50 camera with Olympus U-TV0.5XC-3 and analysed using ImageJ [21] and MATLAB (Mathworks, Natik, US).

NSs: The development of NSs was assessed based on two parameters: (i) the perimeter and (ii) the area of the spheroid. The increase rate was quantified using double exponential fitting (equation (1)):

$$\mathrm{Growth}_{\mathrm{NS}} = Ae^{bt} + Ce^{dt} \tag{1}$$

where the reciprocal of the smaller of the two exponents b or d defines the growth rate (τ_{NS}), and A and C are the coefficients of the fitting equation.

ASs: To determine the optimal day for the ASs formation, we investigated the ratio between the physical contact length between the two NSs to the perimeter of the entire ASs ($\mathrm{contact\ length}/d\pi$). We identified 15% as the ideal value since it represents the midpoint between no contact (and maximum interaction, which occurs when the contact length equals the diameter d of the NSs ($\mathrm{contact\ length} = d: \sim 30\%$).

2.3. MTT assay and cell viability

The cell viability was evaluated by performing the 3-(4,5-dimethylthiazol-2-yl)-2,5-diphenyltetrazolium bromide (MTT) assay every three days from DIV 3 to DIV 21. MTT was added to each well at the final concentration of 0.5 mg ml^{-1} and was removed after 4 h of incubation. The formazan crystals were solubilized using 0.04 M of HCl in isopropanol. The viability of the assemblies was estimated by measuring the absorbance at 570 nm using a microplate reader Agilent technologies Cary 60 UV–Vis spectrophotometer. The analysis of cell viability in 2D cultures was also performed. In this case, the same number of cells used in NSs were plated onto flat 96-well plate precoated with poly-L-ornithine (100 μg ml^{-1}). To quantify cell viability in NSs at each timepoint, their absorbance values were normalized to the mean absorbance of the 2D sister cultures (equation (2)):

$$\mathrm{cell\ viability}_n = \frac{ABS\left(\mathrm{NS}_n\right)}{\overline{ABS}\left(2D_m\right)} \cdot 100 \tag{2}$$

where $ABS(\mathrm{NS}_n)$ is the absorbance of n^{th} NS and $\overline{ABS}\left(2D_m\right)$ is the mean absorbance of 2D samples at each DIV.

2.4. Cell counting protocol

The number of cells within each NS was assessed daily from DIV 0 to DIV 6, and subsequently every three days until DIV 21. NSs were rinsed with HBSS without calcium and magnesium. Then, TrypLE$^{\mathrm{TM}}$ Express reagent was added and incubated at 37 °C for 15 min. To block the dissociation, an equal volume of fresh medium was added. The enzymatic dissociation was followed by a mechanical one with 20 μl pipette tips. The dissociated cells were counted using a hemocytometer and a dilution of cells suspension in 0.04% Trypan Blue in a 1:2 v/v ratio.

2.5. Mechanical characterization

Mechanical properties of the NSs were tested every 3 days from DIV 3 to DIV 21, with a JPK NanoWizard 4 atomic force microscope (AFM) connected to a ZEISS Axio Zoom.V16 microscope. NSs were immobilized on a 35 mm petri dish with the MEA-plating protocol. A spherical-tipped cantilever (40 μm diameter, k $\sim$ 0.27 N m^{-1}) was used to extract information about sample elasticity and morphology. The cantilever sensitivity was computed by performing force curves on glass. For each sample, a 20 × 20 $\mu\mathrm{m}^2$ area was selected, and 8 × 8 measurement points were evenly placed in the area, performing 64 indentation curves per area. Force-displacement curves were acquired with an approach speed of 5 $\mu\mathrm{m\ s}^{-1}$ and maximal target force of 27 nN, resulting in an indentation depth range of 3–11 μm. The elastic modulus was computed using a modified Hertz mode [8, 22] (equation (3)):

$$F(\delta) = \frac{4\sqrt{R}E_{\mathrm{elastic}}}{3\left(1-\nu^2\right)}\delta^{\frac{3}{2}} \tag{3}$$

where δ is the indentation depth (defined by subtracting the cantilever deflection from the z-displacement of the piezoelectric actuator), F the force exerted on the sample, R the effective radius of the cantilever tip, and ν the Poisson's ratio assumed to be 0.5 for incompressible materials.

2.6. Cryosectioning and immunostaining

Every 3 days from DIV 6 to DIV 21, NSs were fixed in 4% paraformaldehyde (PFA) at 4 °C overnight and then washed three times with phosphate buffer solution (PBS) for 1 h each. They were subjected to a gradient of 15% and 45% w v^{-1} sucrose in PBS for 12 h each. NSs were embedded in OCT Compound and stored at −80 °C. 30 μm thick slices were cut using a Leica CM3050 S Cryostat and placed on SuperFrost Plus slides. To restore epitope-antibody reactivity, an antigen retrieval protocol was performed: slices were washed three times with PBS for 10 min each and immersed in Citrate Buffer (10 mM sodium citrate, 0.05% Tween20, pH 6.0) at 95 °C for 10 min. Then, cells were permeabilized and non-specific binding was blocked with a 5% Normal Goat Serum and 0.5% Triton-X100 in PBS solution (PBBS) for 1 h. Samples were incubated overnight at 4 °C in a humidified chamber with anti-GABA (1:500), anti-GFAP (1:500), NeuN (1:500), or MAP2 (1:500) diluted in PBBS. The next day, slices were rinsed twice with a PBS and 0.1% Tween20 solution for 10 min each, followed by a 1 h incubation at room temperature with secondary antibodies (AlexaFluor 488 and AlexaFluor 546) diluted in PBBS (1:700 and 1:1000 respectively). Eventually, after two 10 min PBS washes, samples were exposed to a DAPI solution (1:10 000 in PBS) for 10 min, rinsed twice with PBS, and mounted with Mowiol.

To quantify cell composition within NSs, images were acquired using an Axio Observer 7 microscope mounting an Axiocam 503 mono coupled with a LD Plan-Neofluar 40x/0.6 Corr M27 objective. Five 30 μm-thick slices obtained from distinct spheroids were analysed for each considered configuration. Image analysis was performed using ImageJ and MATLAB for quantitative assessments. DAPI+, NeuN+, GABA+, and GFAP+ cells were manually identified and counted using the Cell Counter Fiji plugin [23]. Neuronal and astrocytic components were expressed as a percentage of the total DAPI-positive nuclei within each image. The number of GABA-positive cells was normalized over the total NeuN-positive population.

2.7. Neuronal cells transfection protocol

To evaluate the structural connections between the NSs, cortical and hippocampal cells were transfected with Amaxa$^{\mathrm{TM}}$ 4D-Nucleofector$^{\mathrm{TM}}$. Briefly, 1 ml of neuronal cell suspension at the concentration of about 4000 cells μl^{-1} was centrifuged at 80 x g at room temperature for 10 min. The supernatant was removed, and neurons were resuspended in 100 μl of room-temperature nucleofection/supplement mixture (82 μl of Nucleofector Solution, 18 μl of supplement, and 2 μg plasmid DNA) by gently pipetting the solution up and down. Then, 100 μl of cell suspension was pipetted into a dedicated nucleofection cuvette and the specific O-0003 program was applied. Cortical neurons were transfected to express green fluorescent protein, while hippocampal neurons were transfected to express red fluorescent protein. The transfected cells were maintained at room temperature for 10 min before cell plating following the procedures indicated above.

2.8. Calcium imaging

Calcium activity of homogeneous and heterogeneous ASs was recorded and analysed at DIV 15, 18, 21. ASs were incubated for 20 min in pH-stable (at 7.4) recording medium with 4.6 μM cell-permeant calcium sensitive dye Fluo-4-AM, 10 mM HEPES, 5.5 mM D-Glucose, 145 mM NaCl, 5 mM KCl, 2 mM $CaCl_2$, and 1 mM $MgSO_4$. Then, ASs were rinsed and placed in a chamber with fresh Fluo-4-free recording medium. The chamber was mounted on Leica TCS SP5 AOBS Tandem DM6000 upright microscope coupled with Leica HCX IRAPO L 25x, 0.95 NA, water objective. Neuronal activity was monitored with high-speed fluorescence imaging using Hamamatsu Orca camera. Calcium imaging was performed at an acquisition rate of 8’000 frames s^{-1}, and the resulting data were temporally averaged to obtain a final effective temporal resolution of 3.8 Hz, allowing reliable detection of spontaneous calcium transients while enhancing signal-to-noise ratio.

The fluorescence intensity traces (F) of detected regions of interest (ROIs) were extracted using the time series analyzer plugin in ImageJ [21]. To improve signal quality, any drift caused by photobleaching was corrected by subtracting it from the signal when fluorescence decay exceeded 15%. Activity events were identified exploiting the Schmitt trigger algorithm [24, 25]. An event was detected when the signal remained between two thresholds for at least 700 ms. Depending on the trace, the upper threshold was set to 10–15 times the standard deviation (std) of the baseline noise, while the lower threshold was set to 5–10 times the same std. A ROI was considered active if it detected at least two events in the 4 min recordings. The macroscopic behaviour of ASs was evaluated in terms of the mean number of events per minute (mean event rate, MER). Synchronization coefficients among ROIs, in the range [0, 1], were obtained using the SPIKE-synchronization algorithm [26]. These coefficients were then clustered with a dendrogram and only those within 80% of the maximum cluster distance were selected for further analysis. Finally, we evaluated inter- and intra-module synchronization for each AS by manually assigning each ROI to one of the two NSs.

2.9. Electrophysiology

The electrophysiological activity of NSs and ASs was recorded for 15 min in spontaneous and for 10 min in

BIC-modulated conditions using the MEA2100 system (Multi Channel Systems, Reutlingen, Germany) and the MC_Rack software with a sampling frequency of 10 kHz. NSs and ASs were immobilized three days prior to recording on the MEA surface with ECM GEL at the final concentration of 4–6 mg ml^{-1}. Working on ice, the gel was applied to the MEAs where the NSs and ASs were then transferred and incubated for 30 min before adding 1 ml of medium. Data were recorded at DIV 15, 18, and 21 outside the incubator. To reduce thermal and mechanical stress during the recordings, MEAs were positioned on a heated pad at 37 °C. A constant flow of humidified gas (5% CO2, 20% O2, 75% N2) was maintained over the MEAs to ensure stable conditions and prevent evaporation or pH shifts in the medium.

Raw data were processed by applying the continuous Gabor wavelet transform, utilizing a logarithmically spaced set of frequencies ranging from 1 Hz to 5,000 Hz. To identify activity events, a threshold TH_i (equation (4)) was computed on the magnitude values obtained from the wavelet transform:

$$\mathrm{TH}_i = c_1 \mathrm{Median}\left(\mathrm{std}_i\right) + c_2 \frac{1}{\mathrm{Max}\left(\mathrm{std}_i\right)} \qquad (4)$$

where Median(std_i) and Max(std_i) represent the median and the maximum stds of the magnitudes computed for the ith frequency, respectively. For each frequency, stds were computed over 250 ms windows with a 100 ms shift between consecutive windows. By increasing c_1, the threshold is raised during periods of high signal variability, indicative of high frequency noise, enhancing sensitivity to fluctuations. c_2 is employed to exclude regions with minimal magnitude changes, corresponding to absence of signal, especially at low frequency. Each electrode in every NSs or ASs was assessed separately. Electrodes exhibiting insufficient activity were excluded in the following unsupervised manner. The area of each recorded event was determined as the product of its temporal duration and its frequency range. These areas were then summed to obtain the total spectrogram area. Then, within each experiment, two thresholds were set to evaluate its pertaining electrodes: the first to 10% of the highest total area, and the second to 75% of the second-largest total area. Electrodes with a total area below the lower of these two thresholds were excluded from the analysis. We specifically investigated the frequencies of the canonical five frequency bands: 1–4 Hz (delta), 4–8 Hz (theta), 8–12 Hz (alpha), 12–35 Hz (beta), and 35–100 Hz (gamma). We quantified the percentage of expression of each frequency interval in every experimental condition in terms of seconds during which the specific band was present.

2.10. Excitation–inhibition (E/I) balance

The analysis of the E/I balance was conducted using the functional E/I (fEI) ratio metric [27]. Each electrode signal underwent band-pass filtering, where the frequency range was determined by including only the frequencies expressed for at least 30% of the duration of the most persistent frequency in that electrode's signal, ensuring that non-characteristic frequency bands were excluded from the analysis. Each filtered signal was then processed to calculate the fEI applying a 30 s window with 80% overlap between windows [27]. The fEI calculation method involves quantifying spectral power and long-range temporal correlations (LRTC)—a scale-free dynamic signature of E/I interactions commonly employed in EEG research. For each band-pass filtered trace, spectral power and LRTC (via detrended fluctuation analysis) were computed and then combined into the fEI ratio: fEI $<$ 1 indicates an inhibition dominated state, fEI $=$ 1 reflects balanced excitation and inhibition, and fEI $>$ 1 denotes an excitation dominated state. This metric was computed for both NSs and ASs under physiological conditions as well as under chemical modulation with Bicuculline at the concentration of 30 μM [28]. At DIV 21, we evaluated the absolute value of the deviation of fEI from the balance (fEI $=$ 1) in physiological and BIC-modulated conditions.

2.11. Statistical analysis

Statistical analyses were performed in MATLAB with the non- parametric Kruskal–Wallis test, as data do not follow a normal distribution (evaluated by the Kolmogorov-Smirnov normality test). Significance levels were set at $p < 0.05$. The box plots representations indicate the 25–75 percentile (box), the std (whiskers), the mean (square), and the median (line) values.

2.12. Dataset

In the present study, a total of 599 NSs (301 C and 298 H) and 293 ASs (88 CC, 108 HH and 97 CH) from 22 preparations were analysed. The entire dataset is reported in Tables (table S40–S44) in the supplementary information.

3. Results

3.1. Morphological, metabolic, and mechanical characterizations prove NSs as a viable and reliable model over time

To assess the morphology and the development of NSs, in cortical (C) and hippocampal (H) configurations, we first compared their perimeter and area during the first 14 days *in vitro* (DIVs) (figures 1(a)–(c)). At DIV 1, cells had not yet assembled into organized structures, especially in C (figure 1(a), top).

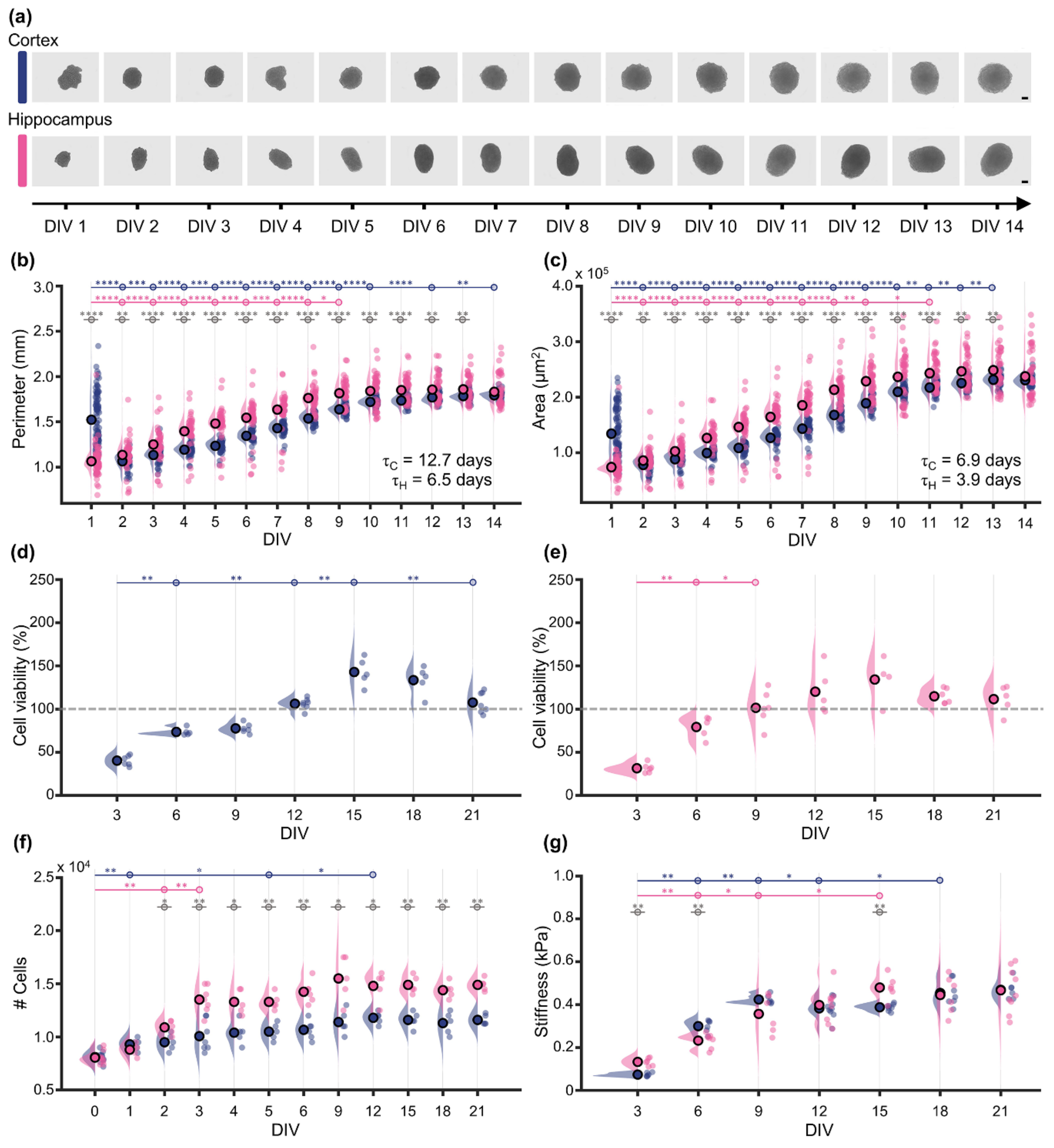

Figure 1. Morphological, metabolic, and mechanical characterization of cortical (C) and hippocampal (H) neurospheroids (NSs) over development. (a) Phase contrast images of two representative C (top) and H (bottom) from DIV 1 to DIV 14. Scale bars, 100 μm. (b) Perimeter and (c) area of C (blue) and H (pink) evaluated from DIV 1 to DIV 14, with τ indicating the C and H growth rate of the corresponding parameter. (d)–(e) Cell viability values of C (blue) and H (pink) from DIV 3 to DIV 21. The grey dotted lines represent the normalized 2D values used as reference. (f) Cell proliferation evaluated in terms of cell number forming C and H from DIV 0 to DIV 21. (g) Stiffness values of C and H from DIV 3 to DIV 21. * refers to $0.01 \leqslant p < 0.05$, ** to $0.001 \leqslant p < 0.01$, *** to $0.0001 \leqslant p < 0.001$, and **** to $p < 0.0001$ by Kruskal–Wallis test. Asterisks are color-coded: blue for C and pink for H differences over development, while the grey ones indicate differences between the two population at the same DIV.

From DIV 2, both populations exhibited monotonic growth; however, the growth rates of perimeter (figure 1(b)) and area (figure 1(c)) in H were approximately twice those of C, as quantified by the time constants (figures 1(b) and (c), insets). This suggests an increased proliferation in H, likely due to a higher presence of progenitor cells (figure S1). After an initial phase of rapid expansion, the increment of both C and H perimeter and area slowed down, albeit at different time points. In C, the trend of the perimeter decelerated at DIV 10 (1.7 ± 0.1 mm), while the area reached a plateau at DIV 13 ($2.3 \pm 0.1 \cdot 10^5$ μm^2). In H, perimeter and area stabilized earlier, at DIV 9 (1.8 ± 0.1 mm) and DIV 11 ($2.4 \pm 0.3 \cdot 10^5$ μm^2), respectively. Significant differences between C and H were observed at each stage up to DIV 13, from when the two populations became comparable geometrically.

As the perimeter and area of the NSs increased over time, it became crucial to assess whether their compact structure might hinder oxygen and nutrient penetration into their core, potentially leading to tissue necrosis [29]. To verify this possible limitation, we investigated the cell viability (according to ISO

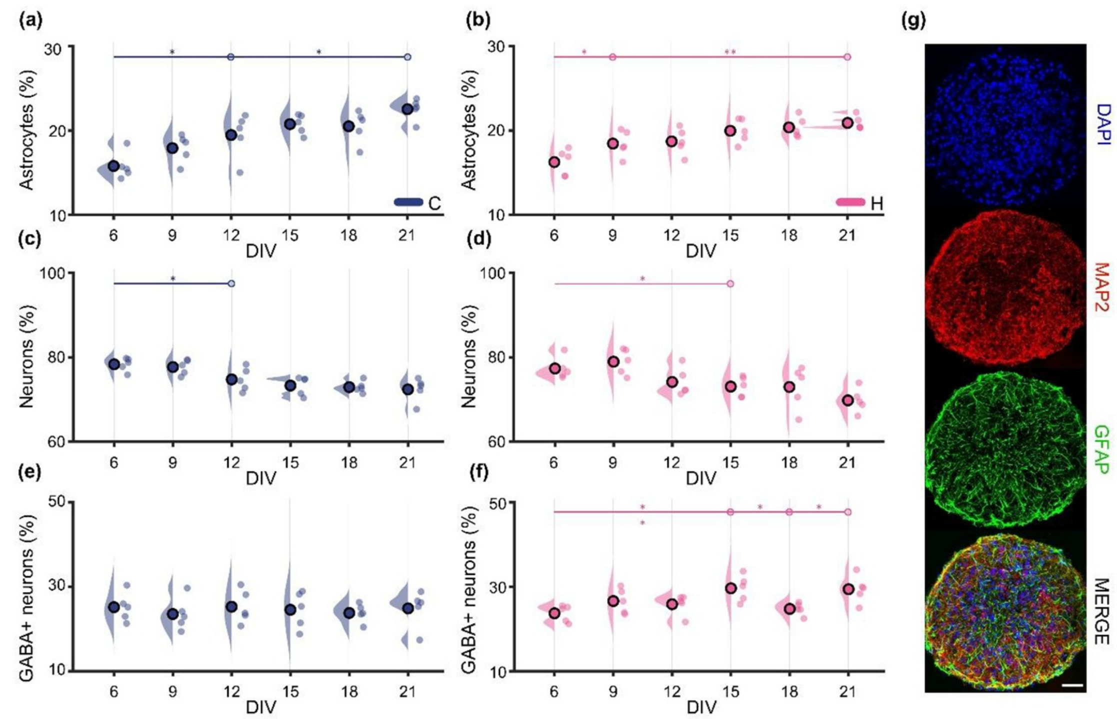

Figure 2. Cell composition analysis of C and H from DIV 6 to DIV 21. Quantitative results showing percentages of glial cells (GFAP+) ((a) and (b)) and neurons (NeuN+) ((c) and (d)) computed over the total number of cells (DAPI+) in C (blue) and H (pink) slices. ((e) and (f)) Percentage of GABAergic neurons (GABA+) computed over the number of neurons (NeuN+) in C (blue) and H (pink) slices. (g) Representative central slice of C at DIV 15 with immunostaining for DAPI (blue), MAP2 (red), and GFAP (green). Scale bar, 50 μm. * refers to $0.01 \leqslant p < 0.05$, ** to $0.001 \leqslant p < 0.01$ by Kruskal–Wallis test. Asterisks are color-coded: blue for C and pink for H differences over development.

10 993-5) of NSs over time using MTT colorimetric assays. We normalized NSs absorbance against that of 2D controls (figures 1(d) and (e)). In the early stages, both C and H exhibited lower cell viability than 2D cultures (cell viability < 100 %) but with an increasing trend. By DIV 12 for C and DIV 9 for H—i.e., around the time when the overall geometry of the structures tended to stabilize—cell viability became comparable to that of 2D (cell viability $= 100\%$), with H exhibiting a faster growth consistent with previous results (figures 1(b) and (c)). At later developmental stages, cell viability in NSs exceeded that of conventional 2D models (cell viability $> 100\%$). This suggested a significant increase in cell number, likely due to more physiological cell–cell interactions and reduced apoptosis, thereby fostering a higher density of synaptic connections [30] and enhancing computation capability [31]. The metabolic increase and the differences in growth rates between the two types of NSs were confirmed through a cell count over development (figure 1(f)). On the day of cell culture preparation, approximately 8'000 cells were seeded per NS and cell proliferation was monitored until DIV 21. Consistent with their geometry, H contained a significantly higher number of cells compared to C already from DIV 2. This trend was maintained throughout development, with H reaching a peak value before C (DIV 9 for H with an average 15'500 ± 2'121 cells and DIV 12 for C with an average of 11800 ± 570 cells).

The greater cell proliferation in NSs (compared to 2D cultures) and the NSs morphology might be influenced by the models' mechanical properties, which have a crucial role in neuronal function and development [32]. Therefore, we evaluated NSs Young's modulus from DIV 3 (0.07 ± 0.01 kPa for C and 0.13 ± 0.02 kPa for H) to DIV 21 (0.47 ± 0.05 kPa for C and 0.47 ± 0.10 kPa for H). As for previous findings, both C and H exhibited an increasing stiffness over time, with values progressively aligning with *in vivo* [33] (0.3–1 kPa, figure 1(g)). Along with geometrical considerations, this gradual shift towards native tissue mechanical properties, as opposed to the much harder surfaces used in 2D cultures, might have contributed to the higher observed cell viability (figures 1(d) and (e)).

The cellular composition of NSs is a critical marker of their physiological relevance as the balance between distinct neuronal cell types deeply influences neuronal function, dynamics [34], and viability [35]. With immunocytochemical analysis, we studied the composition of NSs and the spatial organization of neuronal and glial populations in C and H over time (DIV 6–21). The GFAP+ component displayed a significant, progressive increase (reaching 22.5 ± 1.3% in C and 20.9 ± 0.8% in H at DIV 21, figures 2(a) and (b)). The first statistical difference emerged at DIV 12 in C and DIV 9 in H. The NeuN+ population generally followed an opposite trend (figures 2(c) and (d)),

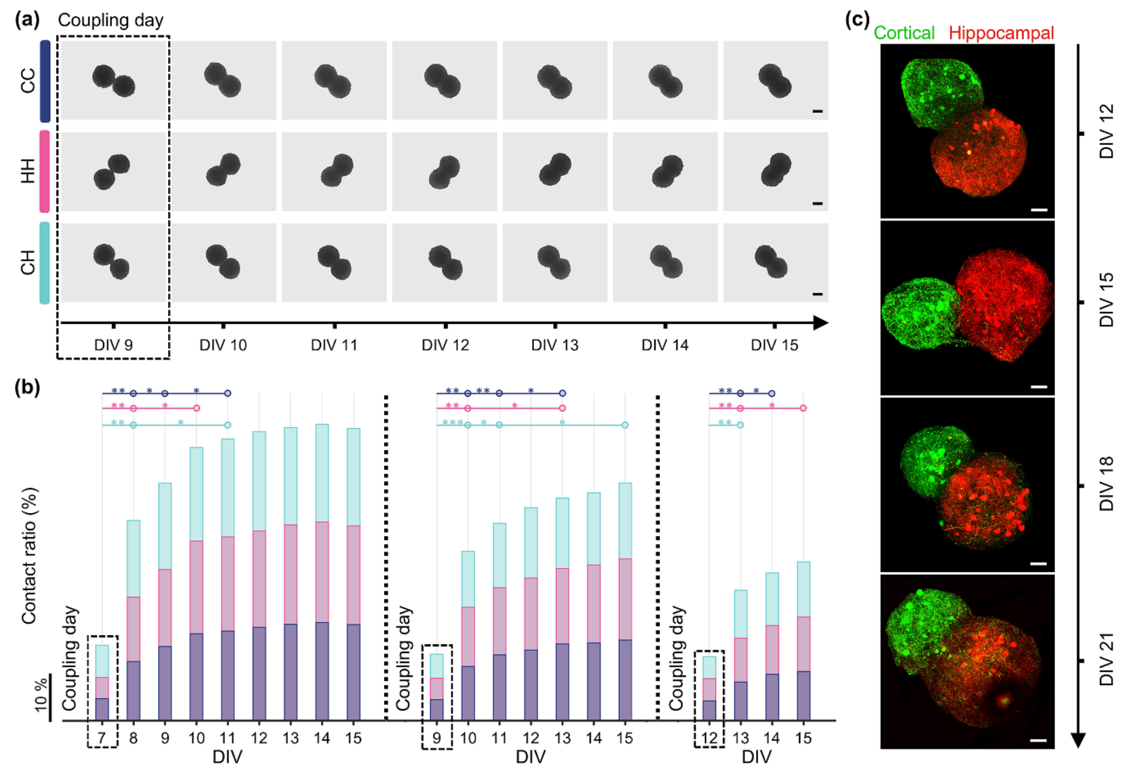

Figure 3. Morphological characterization of assembloid-like structures (ASs) in different configurations: cortical–cortical (CC), hippocampal–hippocampal (HH), and cortical–hippocampal (CH). (a) Phase contrast images of representative CC (top), HH (middle), and CH (bottom) from DIV 9 (coupling day) to DIV 15. Scale bars, 200 µm. (b) Ratio (percentage) of the physical contact length between the two NSs to the entire AS perimeter of CC (blue), HH (pink), and CH (light blue) coupled at DIV 7, 9, 12. * refers to $0.01 \leqslant p < 0.05$, ** to $0.001 \leqslant p < 0.01$, *** to $0.0001 \leqslant p < 0.001$ by Kruskal–Wallis test. Asterisks are color-coded: blue for CC, pink for HH, light blue for CH. (c) Confocal z-stack images of transfected CH (coupled at DIV 9) acquired at DIV 12, 15, 18, 21. Cortical and hippocampal neurons are color-coded in green and red, respectively. Scale bars, 50 µm.

stabilizing at DIV 12 in C (74.7 ± 2.7%) and at 15 in H (73.1 ± 2.4%), reflecting the physiological astrocyte-to-neuron ratio [36]. Furthermore, we evaluated the proportion of inhibitory neurons, quantifying the number of GABAergic ones (figures 2(e) and (f)). In C, the fraction of GABA+ cells remained constant (24.9 ± 4.4% at DIV 21, figure 2(e)), suggesting early stabilization of the inhibitory population. Contrarily, H exhibited a gradual increase in GABAergic neurons (29.4 ± 3.3% at DIV 21, figure 2(f)). Despite the differences, the percentage of inhibitory cells closely approximated physiological levels in both conditions [37, 38]. Additionally, DAPI staining revealed a homogeneous nuclear distribution, a finding reflected in astrocytes behaviour, whereas neuronal cells exhibited a preferential localization along the periphery (figure 2(g)). Still, the presence of well-developed dendritic processes suggests the presence of viable neuronal cells throughout the entire NS.

3.2. ASs morphological characterization reveals robust interconnection between segregated populations

To investigate the interregional communication and dynamic processes among neuronal populations, we aimed to create a 3D model of the cortical–hippocampal circuit based on ASs. Coupling NSs at different developmental stages can drive their interaction, leading to the formation of distinct but not-trivially connected modules within the ASs. We inferred that NSs reach an advanced maturation stage between DIV 9 and 10 in terms of cell viability, number of cells, and overall size (figure 1). Thus, we combined cortical and hippocampal NSs into either cortical (CC), hippocampal (HH), or heterogeneous cortical–hippocampal (CH) ASs from DIV 7 to DIV 12 to test ASs formation efficacy (figure 3(a)). To derive the optimal coupling day, we evaluated the ratio of the physical contact length between the two NSs to the perimeter of the entire ASs (figures 3(b) and S2(a)). The trend of contact ratio was similar for all considered coupling days and across all configurations, i.e., it doubled or tripled the day after coupling and steadily increased afterwards (figures 3(b) and S2(a)). However, the level of morphological interaction between NSs coupled at different DIVs was different.

The highest contact percentage was reached if they were coupled at DIV 7. The values (20.0 ± 2.3% in CC, 20.5 ± 2.6% in HH, 20.3 ± 2.4% in CH, figure 3(b), left) indicate that this condi-

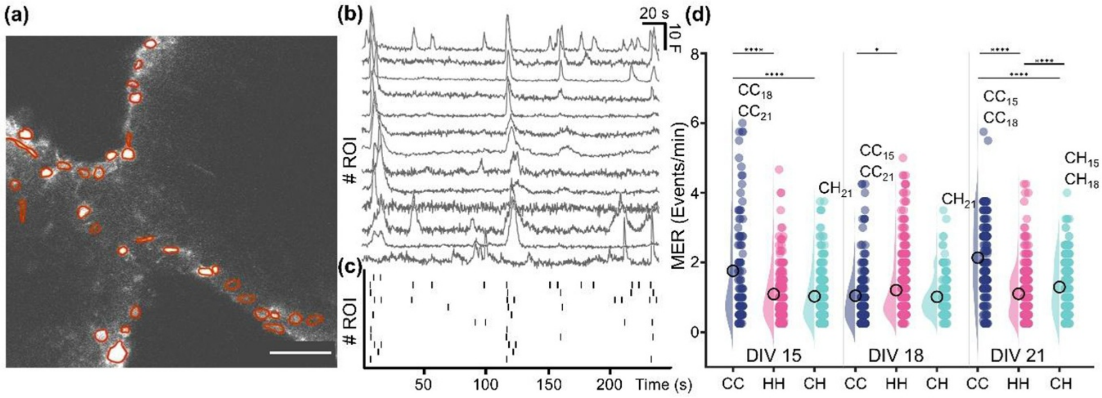

Figure 4. Calcium activity recorded over time. (a) Representative frame of a HH contact area at DIV 18. Regions of interest (ROIs) are highlighted in red. Scale bar, 50 µm. (b) Relative Ca2+ activity traces from the detected ROIs and (c) relative raster plot. (d) Mean event rate (MER, events/min) of CC (blue), HH (pink), and CH (light blue) at DIV 15, 18, 21. The acronyms indicate a $p < 0.05$ in the statistical comparison among congruent ASs at different DIVs. * refers to $0.01 \leqslant p < 0.05$, ** to $0.001 \leqslant p < 0.01$, *** to $0.0001 \leqslant p < 0.001$, and **** to $p < 0.0001$ by Kruskal–Wallis test.

tion promoted the formation of multiple structural connections between NSs, but it also resulted in insufficient segregation between the two modules. Contrarily, NSs coupled at DIV 12 failed to establish enough inter-module connections to form cohesive structures as indicated by the low contact ratio over time (at most 10.0 ± 1.0% in CC, 11.1 ± 1.2% in HH, 11.3 ± 1.0% in CH, figure 3(b), *right*). This falls in line with the observation that at DIV 12 the NSs had already reached a more mature developmental stage (figure 1). Conversely, coupling at DIV 9 promoted the growth of robust physical connections while maintaining clearly defined separated modules within the ASs. ASs formed at this stage of development (figure 3(a)) reached maximum interaction four and six days after coupling in homogeneous and heterogeneous configurations, respectively. The intermediate percentages of contact ratio (at most 16.4 ± 1.5% in CC, 16.5 ± 2.9% in HH, 15.5 ± 1.9% in CH, figure 3(b), centre) were sufficiently high to ensure structural integrity to the ASs while preserving the distinguishability between NSs. Therefore, DIV 9 was chosen as the best coupling day for all subsequent analyses.

To further support these observations, we explored the structural components using a transfection technique to express differently labelled proteins in the NSs of representative CH samples coupled at DIV 9 (figures 3(c) and S2(b)). We assessed the structural inter-module projections at DIV 12, 15, 18, and 21. At DIV 12, the structural inter-module connections were restricted to the contact area (figure 3(c) and S2(b)). By DIV 15, some cortical links began to extend into the hippocampal module, becoming increasingly prominent at DIV 18. At DIV 21, the structural connections from both populations were able to fully interconnect the two NSs while preserving their segregation. Notably, the confocal images provide evidence that the neurites of the cortical module structurally extend into the hippocampal population, possibly reflecting the *in vivo* organization of these brain regions (figure S2(b)) [39, 40].

3.3. Calcium imaging proves functional interconnection and reveals synchronization dynamics in ASs

From a morphological and structural perspective, we identified DIV 9 as the optimal coupling day to obtain ASs with robust physical connections between distinct, segregated modules over time. To determine whether these structural links (figure 3) had functional confirmation, we analysed the electrophysiological activity of the ASs throughout maturation (every 3 days from DIV 15–21) with calcium imaging. ASs activity was monitored at the junction of the two NSs to focus the investigation on their interaction (figure 4(a)). Fluorescent traces were recorded (figure 4(b)) and neural events detected (figure 4(c)). Firstly, we investigated the activity of ASs in terms of MER as a function of their development (figure 4(d)).

The HH configuration displayed stable MER throughout the recordings, whereas CC exhibited a higher event rate and greater variability at DIV 15 and 21. CH closely mimicked the behaviour of HH at DIV 15 and 18; however, at DIV 21, MER significantly increased reaching an intermediate value between HH and CC, likely due to the influence of the cortical module. By DIV 21, each configuration seemed to exhibit a distinct pattern of neural activity, possibly indicating unique maturation dynamics across different AS models.

Next, to explore the information transmission between the NSs, we quantified the synchronization levels (figures 5(a)–(d)), identifying patterns both within and between modules of each AS. Overall, we observed a global increase in the syn-

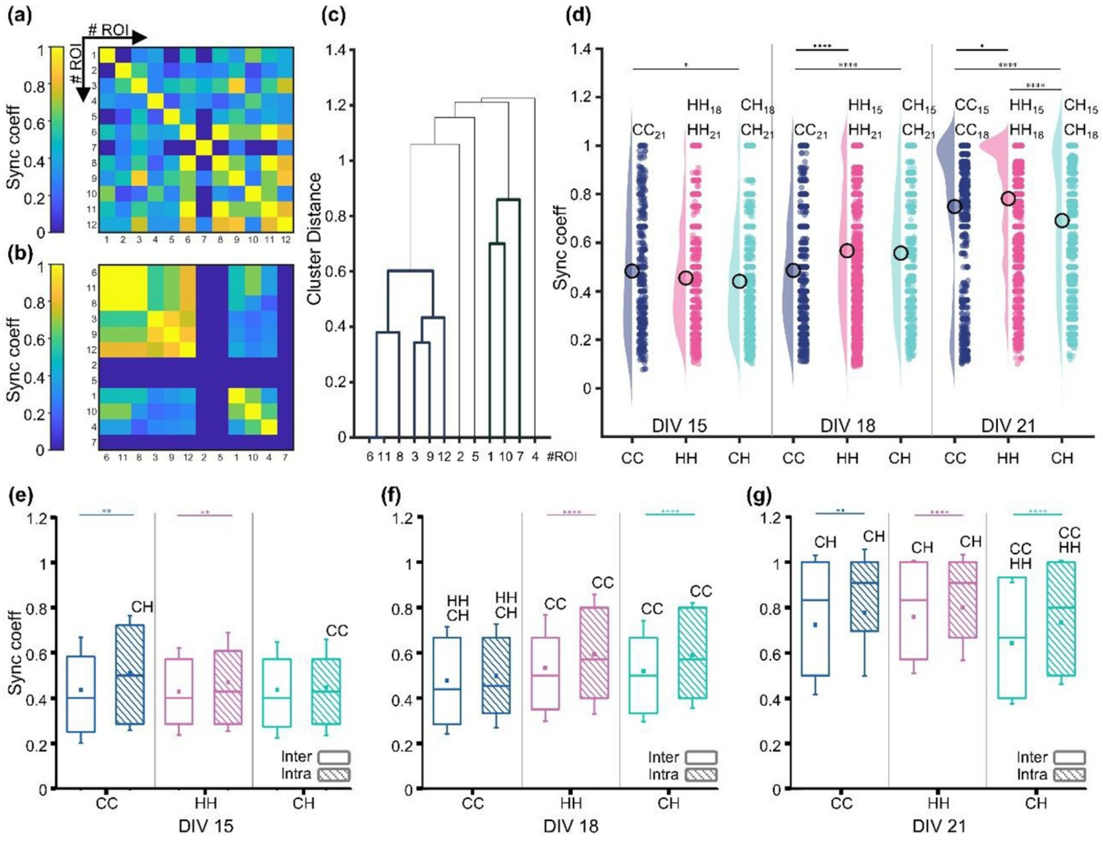

Figure 5. Global, inter-, and intra-module synchronization coefficients in assembloid-like structures. (a) Synchronization coefficients matrix of ROIs activity of the representative HH at DIV 18 depicted in figure 4(a). (b) Reordered matrices according to the cluster distance dendrogram in (c). The threshold used for cluster separation is 80% of the maximum dendrogram value. (d) Global synchronization coefficients of CC (blue), HH (pink) and CH (light blue) at DIV 15, 18, 21. The acronyms indicate a $p < 0.05$ in the statistical comparison among congruent ASs at a different DIVs. ((e), (f) and (g)) Inter- and intra-module synchronization coefficients at DIV 15, 18, 21. The acronyms indicate a $p < 0.05$ in the statistical comparison between inter- or intra-module synchronization values in different ASs configuration. * refers to $0.01 \leqslant p < 0.05$, ** to $0.001 \leqslant p < 0.01$, *** to $0.0001 \leqslant p < 0.001$, and **** to $p < 0.0001$ by Kruskal–Wallis test.

chronization levels over time in all configurations, though the trend differed among them. The increment was delayed but steeper in CC, which started as the most synchronous configuration. In contrast, CH and HH levels showed a gradual increase at each recording point, exhibiting similar synchronization profiles up to DIV 21 (figure 5(d)), when CH exhibited lower synchronization coefficients than both CC and HH. Considering the position of the ROIs and decomposing their contribution to the synchronization levels, we observed that the intra-module coefficients were consistently higher than those between modules, albeit not always in a statistical way (figures 5(e)–(g)). At DIV 15, the higher synchronization level observed in CC (figure 5(d)) was primarily driven by the intra-module coefficients (figure 5(e)). In the physiological CH configuration, similar intra- and inter-module synchronization levels at the junction could indicate a strong interaction between the NSs at this stage of development. By DIV 18, both the inter- and intra-module coefficients in HH and CH increased, surpassing those observed in CC (figure 5(f)). The largest increment was observed for both CH and HH in intra-module synchronization, with values significantly higher than those between NSs (figure 5(f)). At DIV 21, all configurations exhibited lower inter-module synchronization (figure 5(g)). This fact may suggest that the individual populations retain their distinct identities throughout development despite effective communication between them, a feature that could be particularly relevant in the CH configuration.

3.4. NSs and ASs display brain rhythms and a physiological excitatory/inhibitory balance

We examined the patterns of electrophysiological activity in terms of oscillatory rhythms, which are typically recorded *in vivo*, to verify whether our model was able to induce their generation. MEAs were used to collect signals from NSs and ASs and extract the spectrograms (figure 6(a)). We quantified the expression of the different brain waves (i.e., the percentage of occurrences evaluated as seconds during which the specific band was present) in each configuration at DIV 15, 18, and 21 (figures 6(b), (c) and S3). Alpha rhythm (8–12 Hz, figure 6(b), third column) was consistently present throughout development

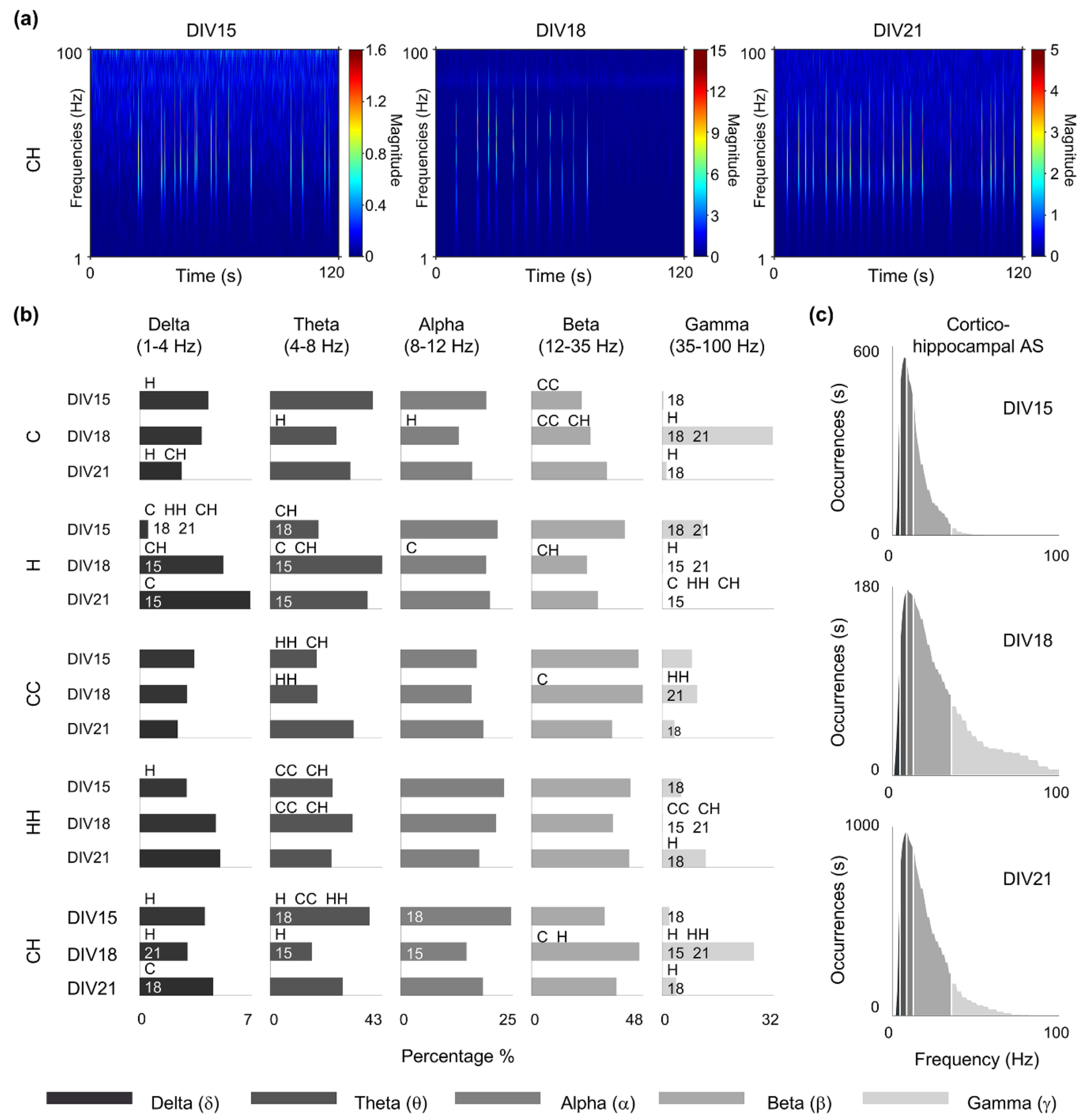

Figure 6. Brain waves expression in NSs and ASs. (a) Spectrograms of representative CH samples at DIV 15, 18 and 21. The colormap indicates the magnitude. (b) Bar plots showing the mean percentage of expression of delta, theta, alpha, beta, and gamma rhythms at DIV 15, 18 and 21 in C (first row), H (second row), CC (third row), HH (fourth row), and CH (fifth row). The greyscale shading identifies the different bands. The acronyms and numbers superimposed on the bars indicate a $p < 0.05$ by Kruskal–Wallis test in the statistical comparison among configurations at the same DIV (acronyms) and among congruent configurations at different DIVs (numbers). (c) Histograms of representative CH samples showing the duration of frequency contributions corresponding to delta, theta, alpha, beta, and gamma brain waves. Each grey area provides an indication about the level of expression of the wave in the 3D model.

(figures 6(b) , (c) and S3). These waves showed the highest expression at DIV 15 across all configurations except for CC, which exhibited a slight increase at DIV 21. In hippocampal constructs (H, HH), they typically remained stable or decreased gradually over time. Contrarily, C and CH featured a decreased expression at DIV 18 and stabilized on an intermediate value by DIV 21.

The lowest detected frequency rhythms were not particularly present in our model: delta waves (1–4 Hz, figure 6(b), first column) accounted for at most 7% of the global wave expression across all configurations (figures 6(b), (c) and S3). In cortical constructs (C, CC), these waves decreased monotonically from DIV 15–21, coinciding with an increase in higher-frequency waves such as beta and gamma. In contrast, in hippocampal configurations (H, HH) delta rhythm became more pronounced, particularly from DIV 15 to DIV 18. CH differed from the other configurations, with a decrease in delta wave expression at DIV 18, reaching levels similar to CC, before becoming more prominent at DIV 21, with percentages comparable to HH.

Theta rhythm (4–8 Hz, figure 6(b), second column) increased its expression from DIV 15–18 in hippocampal constructs (H, HH), statistically in the

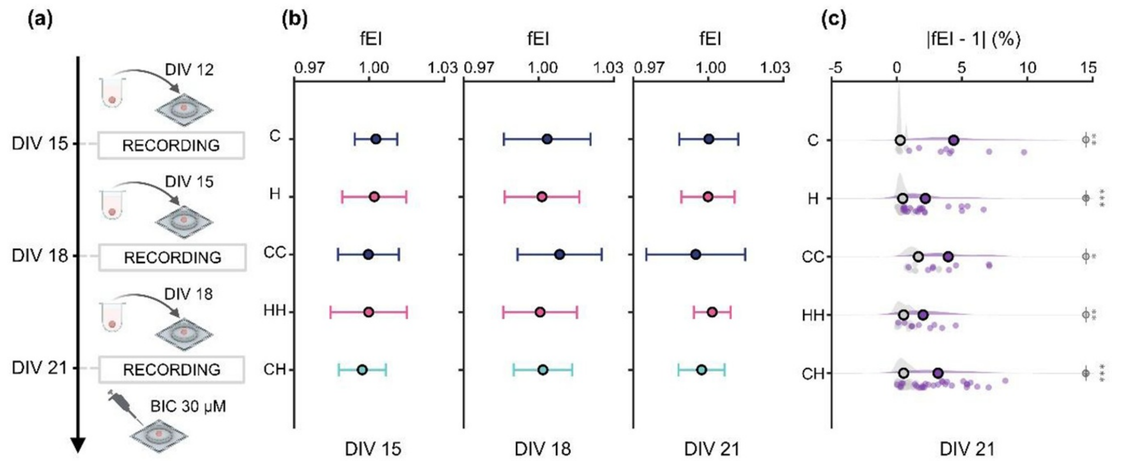

Figure 7. Functional Excitatory/Inhibitory (E/I) ratio. (a) Schematics of data collection timeline. (b) Distribution of the functional excitatory/inhibitory ratio (fEI) across different neuronal configurations at DIV 15, 18, and 21. fEI values around 1 indicate a balance between excitation and inhibition. (c) Deviation of fEI values from the balance (~ 1) in physiological (grey) and BIC-modulated (purple) conditions at DIV 21. BIC was delivered at 30 µM. * refers to $0.01 \leqslant p < 0.05$, ** to $0.001 \leqslant p < 0.01$, *** to $0.0001 \leqslant p < 0.001$, and **** to $p < 0.0001$ by Kruskal–Wallis test.

case of H. Subsequently, theta levels decreased, with the HH condition returning to its initial value by DIV 21. Conversely, C and CH exhibited their highest theta expression at DIV 15, followed by a decrease at DIV 18 and a slight rebound at DIV 21. Finally, the CC configuration presented an increasing trend on the last day.

The expression of theta waves exhibited a complementary trend to beta's (12–35 Hz, figure 6(b), fourth column) for all the configurations except for C at DIV 21. In this case, both waves showed a slight increase with respect to DIV 18, reaching comparable percentages that were balanced by a sharp decline in gamma activity. Interestingly, beta rhythm was generally more present in complex structures (i.e., the ASs), especially in CC and HH where it was the most expressed rhythm (figures 6(b) and S3). In the heterogeneous case, at DIV 15, beta waves were less prominent than H, but their level increased, peaking at DIV 18, and stabilizing at an intermediate value by DIV 21. Finally, the expression of gamma waves (35–100 Hz, figure 6(b), fifth column) did not follow a well-defined trend (figures 6(c) and S3). In hippocampal configurations (H and HH), gamma rhythm tended to disappear at DIV 18. In contrast, cortical and heterogeneous configurations (C, CC, and CH) featured a peak in gamma activity at DIV 18, although values were not stable over time.

Focusing on the heterogeneous configuration (CH, figure 6(b), fifth row), we observed a marked shift in the expression of all waves at DIV 18 (figure 6(b) and (c)) with respect to DIV 15. There was a reduction in delta, theta, and alpha oscillations, with a parallel increase in faster oscillations like beta and gamma. At this stage (DIV 18), CH tended to follow the same wave expression of CC, except for gamma, which was more present in CH. Conversely, at DIV 21, the expression patterns of all waves reversed. CH percentages stabilized at intermediate values between those at DIV 15 and 18 in the same configuration, and between those at DIV 21 in HH and CC. These fluctuations suggest that DIV 18 represents a critical time point for network reorganization, followed by the stabilization of oscillatory dynamics by DIV 21.

The analysis of the characteristic frequency bands of the signal allows for the extraction of the fEI ratio [27] that quantifies the dynamical state of the networks and provides indications about possible alterations. We confirmed that the E/I balance was properly established under physiological conditions both in NSs and ASs, with fEI values remaining consistently close to 1 across all configurations over time (figures 7(a) and (b)), a condition expected as the GABA switch finishes by DIV 13 in rat cultures [41–43]. Then, at DIV 21, we delivered Bicuculline (BIC), a $\mathrm{GABA_A}$ receptor antagonist, at 30 μM to verify that an induced E/I imbalance would alter the fEI (figure 7(a)). All the considered configurations displayed a significant sensitivity to the delivery of BIC, which shifted and spread their fEI from physiological values (grey curve) towards unbalanced conditions (purple curves) (figure 7(c)).

4. Discussion

Understanding how distinct brain regions interact structurally and functionally remains one of the major challenges in neuroscience. *In vitro* 2D neuronal networks have significantly contributed to our knowledge of brain function and disease mechanisms [44, 45]. However, these models often fail to accurately reflect the complexity of the brain as they lack 3D and heterogeneity, impairing their physiological relevance [46–48]. To address this issue, recent efforts have turned toward 3D models, such as NSs [5], organoids [11], and assembloid or ASs, which offer a more physiologically relevant microenvironment [12, 15].

In this context, we introduce a simplified and experimentally tractable 3D *in vitro* system designed to study structural and functional interactions between distinct brain regions using modular cortical and hippocampal NSs. Rather than mimicking the *in vivo* circuitry in its entirety, our model focuses on offering precise control over inter-regional coupling and maturation timing, facilitating the investigation of emergent network features under well-defined conditions. Our work complements and extends prior 3D systems by using a scaffold-free modular assembly, enabling spontaneous yet reproducible interconnectivity. We implemented the model using a conventional fusion method based on ultra-low attachment U-bottom well plates, thereby maintaining a fully scaffold-free environment: no external biological or synthetic matrices (e.g., Matrigel, PDMS, collagen, chitosan [3, 19, 49, 50]) were used during the formation and maturation of both single spheroids and assembled constructs. This enabled the spontaneous self-organization of 3D structures without physical constraints or guided positioning. More engineered systems—such as microfluidic platforms—can offer fine control over connectivity and axonal guidance [51], allowing direct resolution of axonal conduction or transmission dynamics. They have been shown to play a critical role in coordinating oscillatory behaviour across interconnected modules, influencing burst timing, synchronization, and neuronal maturation [52]. However, these systems often require more complex setups and prolonged culture on rigid flat substrates, which may affect 3D architecture, limit imaging access, and reduce scalability [53]. In contrast, our setup favours a simplified and flexible design, well-suited for multimodal analysis across structural and functional domains.

While previous assembloid studies have often relied on human stem cell-derived systems [12–14], which present batch-to-batch differences and long differentiation timescales, we focus on NSs and ASs derived from primary rodent neurons to reduce variability and increase throughput. Our modular approach supports physical integration and allows for reproducible pairing of spheroids at defined developmental stages, facilitating the study of heterochronic interactions and inter-regional connectivity. Such experimental control is often difficult to achieve in organoid-based systems, where variability in size, shape, and differentiation state can confound functional readouts [54]. This positions our approach as a pragmatic bridge between traditional 2D cultures and complex organoid systems, particularly suited for high-throughput applications such as pharmacological screening or biophysical manipulations. Our findings, therefore, align with and contribute to current efforts at balancing biological complexity with tractability—an increasingly important consideration for both basic neuroscience and preclinical platforms.

We characterized the proposed 3D model using a multimodal approach to ensure a comprehensive assessment across structural and functional domains. Morphological analysis revealed distinct and consistent growth trajectories for cortical (C) and hippocampal (H) spheroids (figures 1(b) and (c)), mirroring known *in vivo* differences in neurodevelopmental timing and plasticity [55]. Complementing these region-specific patterns, both spheroid types displayed progressive increase in stiffness over time (figure 1(g)), with values gradually approaching those of native brain tissue [33]. This shared mechanical maturation not only supports the emergence of biomimetic properties in the system but is also fundamental for the correct expression of underlying neurodevelopmental processes—such as neuronal migration, astrocyte organization, and inhibitory circuit formation [8, 56, 57]—that are often disrupted in planar models. Although expected, these parallel trends offer a valuable experimental framework for exploring region-specific network development under precisely controlled and reproducible conditions.

To determine whether these mechanical changes corresponded to a biologically meaningful architecture, we next performed immunostaining (figure 2). Astrocytes and neurons followed temporally distinct developmental trajectories, with astrocytic proliferation beginning earlier in hippocampal than cortical spheroids. This offset mirrors the earlier mechanical stabilization observed in H and supports literature linking extracellular mechanics to astrocytes regulation of synaptic function and trophic support [58]. Notably, the overall astrocytes-to-neuron ratio ($\sim$ 25/75) aligned well with physiological benchmarks [36], and spatial compartmentalization of neurons and astrocytes emerged spontaneously, with neurons predominantly localizing to the periphery and astrocytes being more uniformly distributed throughout the spheroid (figure 2(g)). This suggests that even in a simplified model, cell populations may self-organize in response to intrinsic metabolic demands [59] and nutrient gradients, optimizing conditions for variability and signal transmission. These architectural adaptations were functionally validated by metabolic assays showing that viability in 3D cultures surpassed that of their 2D counterparts, particularly after the DIV 9–12 transition period (figures 1(d) and (e)). This developmental window also corresponded to peak proliferation in both C and H spheroids (figure 1(f)), reinforcing its importance as a pivotal stage in circuit emergence. While similar dynamic transitions have been documented in prior studies of 2D neuronal networks (refs), our model enables to explore them within a 3D context that better preserves spatial organization and cell-type interactions. The ability to define and manipulate such critical periods with precision is a key advantage of our approach. It opens avenues for targeted interventions—pharmacological, genetic, or environmental—at developmentally relevant stages.

Calcium imaging was employed to assess the functional relevance of the structural connections between spheroids. Activity dynamics appeared to show differences by configuration. Both CH and HH maintained a relatively stable MER at earlier time points. By DIV 21, however, only CH exhibited an increase in MER. This trend may reflect the contribution of the cortical component, as also suggested by the increased CC activity at this later stage (figure 4(d)). These differences underscore the role of spatial arrangement and neural identity in shaping network evolution, extending to a 3D modular framework that supports structured interregional coupling findings reported in co-cultured 2D systems [60]. Synchronization analysis further revealed a progressive increase in coordinated activity across all configurations (figure 5). Notably, intra-module synchronization consistently exceeded inter-module values (figures 5(e)–(g)), indicating that the functional specificity of the original spheroids was preserved despite their physical integration. This pattern aligns with structural observations (figure 3) and supports the idea that ASs formed under controlled coupling conditions retain distinct population-level identities. This modular organization may confer computational advantages such as improved signal segregation, robustness to local perturbations, and support for parallel processing—principles of both biological and artificial neural networks [31, 61]. The sustained predominance of intra-spheroid synchrony also parallels brain developmental processes, where local microcircuits form and stabilize before large-scale interregional integration occurs [62]. In this context, the observed delay in inter-module synchrony may reflect a biologically relevant progression from local to global network organization. It is important to note that Fluo-4 (the calcium indicator used in this study) is a non-specific dye that labels both neurons and glial cells [63]. Nevertheless, Fluo-4 has been widely employed to monitor neural activity in various contexts, including studies of network dynamics [64], assessments of functional connectivity [65, 66], investigations linking connectivity with resilience to perturbations and pharmacological modulation [41, 67], evaluations of novel stimulation platforms [68], analyses of oscillatory behaviour [41], and disease modelling [69]. While the non-specificity of the dye was taken into account when interpreting our results, we also considered the substantial body of evidence supporting its effectiveness in evaluating neural cultures and their maturation, a process involving both neuronal and glial components.

Finally, to explore whether the configuration-dependent differences in activity patterns observed via calcium imaging extended to the frequency domain, we performed spectral analysis of the electrophysiological recordings. Multiple frequency bands emerged across all AS configurations (figure 6), suggesting the presence of distinct dynamic states throughout development. Alpha waves, which are implicated in perceptual events gating and coordination of interregional communication [70, 71], were consistently detected in our models. Theta rhythm, typically associated with hippocampal processing and large-scale integration [72, 73], showed a transient peak at DIV 18 in our hippocampal constructs before declining. This temporal profile may reflect synaptic reorganization. Beta-band activity, linked to long-range communication and cognitive processes [74, 75], was more prominent in the more complex assembloid-like configurations. Theta and beta waves often followed complementary patterns, in line with prior reports of their competitive or sequential expression during maturation or task-relevant states. Gamma oscillations were detected in all configurations but exhibited brief and variable patterns, with construct-specific differences in temporal dynamics. A marked expression change was observed at DIV 18, suggesting a modulation in local network organization. This interpretation aligns with previous evidence that *in vitro* gamma oscillations are shaped by microcircuit architecture [76], and that *in vivo* gamma rhythms typically occur in brief bursts [72], supporting high-level local processing through precise temporal synchrony and coordination [73, 75, 77, 78]. A particularly notable finding is the marked shift in overall oscillatory dynamics at DIV 18 in the most complex configuration (CH), evolving from slow (delta, theta, alpha) to fast (beta, gamma) oscillations. This transition typically marks key developmental stages [79], suggesting increasing integration within the network. These results support the idea that DIV 18 represents a critical network maturation phase, after which oscillatory activity stabilizes.

These results place our model within the broader landscape of *in vitro* systems investigating the emergence of neural rhythms, while highlighting key advantages in terms of maturation speed, modularity, and circuit-level organization. Research using 2D primary neuronal cultures has provided valuable insights into intrinsic network states, studying oscillatory activity (e.g., in the theta range) emerging under both baseline and pharmacologically manipulated conditions [41]. In parallel, spatially organized neuronal clusters on MEAs have demonstrated that even small aggregates (as few as 40 cells) can generate spontaneous high-frequency oscillations (25–100 Hz), shaped by inhibitory signalling and structural parameters such as cluster size and connectivity [80]. These studies underscored the importance of topological features in shaping oscillatory behaviour, yet they lack the 3D architecture and region-specific features of brain tissue that critically influence network connectivity. Moreover, they also highlighted the need to explore the electrophysiological properties of interconnected clusters—an open question directly addressed by our model. More recently, organoid-based systems have added biological richness, showing the capacity to generate structured oscillatory patterns—including delta and theta rhythms, and theta-gamma phase-amplitude coupling—over extended periods of maturation [52, 81]. However, these dynamics typically require weeks to months to emerge and often display high inter-batch variability. In contrast, our 3D models effectively bridge the gap between the fast-developing 2D cultures and the structural complexity of organoid systems, replicating transitions in oscillatory regimes typically observed in human 3D models but within a much shorter timeframe. Our ASs provide an experimentally accessible and physiologically relevant system to dissect how spatially distinct neuronal populations generate coordinated oscillatory activity and to probe the interplay between network architecture and functional dynamics—addressing key drawbacks in current *in vitro* models.

Despite providing valuable insights into the emergence of oscillatory activity within interconnected regions, certain limitations of our systems should be acknowledged. The reliance on 2D under-sampling, albeit partially compensated by multi-plane calcium imaging, restricts a comprehensive reconstruction of the full 3D network connectivity. Additionally, the absence of a controlled external electrical stimulation reduces our ability to dissect and characterize stimulus-specific responses within and across modules. Moreover, our functional redouts primarily capture somatic activity, without resolving cellular processes such as axonal conduction or synaptic transmission. Such detailed insights are only accessible through the integration of advanced technologies, including microfluidic compartmentalization, which enable finer dissection of information flow across circuits [51, 52].

Although these constraints remain, our findings still demonstrate the potential of our model to unravel fundamental mechanisms underlying network oscillations and their role in neuronal computation and brain development [82]. It is indeed a tractable system to probe how neuronal coding emerges from the interaction of discrete modules. This dynamic interplay suggests a potential refinement of the theory of state-dependent information processing [83, 84], framed within an AS-based computational paradigm, in which intrinsic dynamic states are shaped by region-specific interactions (figures 5 and 6).

To further explore the principles underlying these dynamics, we evaluated the E/I balance using the fEI metric—a rhythm-derived measure sensitive to changes in synaptic connectivity and inhibitory signalling [27]. Under baseline conditions, fEI remained near equilibrium for all NSs and ASs (figure 7(c), grey), indicating a stable and well-balanced network state. This evidence is consistent with morphological findings of inhibitory neuron proportions (∼25–30%) aligning with *in vivo* physiological benchmarks [37, 38]. This parallel confirmation further validates the model's structural and functional relevance (figures 2(e) and (f)). Pharmacological manipulation of inhibitory signalling pathways induced significant shifts in fEI (figure 7(c), purple). These changes underscored the model's responsiveness to E/I fluctuations and its relevance for modelling pathological disruptions in network balance, such as those implicated in epilepsy [85].

In summary, our ASs offer a simplified yet physiologically relevant platform for investigating inter-regional interactions under controlled and reproducible conditions. By integrating structural, mechanical, and functional readouts, the model captures key aspects of neural circuit development—including configuration-dependent dynamics, progressive synchronization, and the emergence of oscillatory states—within a framework that is experimentally accessible and scalable. Moreover, the system's modular organization, with physically coupled but functionally distinct compartments, enables selective targeting of individual spheroids without compromising the overall connectivity. This opens the door to precise experimental manipulation at the regional level and to localized perturbation strategies aimed at probing causality within coupled networks. To illustrate this potential, we implemented a proof-of-concept selective targeting using a nanoparticle-based delivery strategy designed to achieve region-specific drug exposure. We adapted the protocol developed by Huang and colleagues [86] to synthesize PLGA/PVA nanoparticles, and we further coated them with laminin and fluorescent poly-L-lysine to promote neural adhesion and tracking [87] (figure 8(a)). They were introduced into one single spheroid at DIV 8 (either C or H), followed by coupling to an untreated counterpart at DIV 9 and fixation at DIV 15 (figure 8(b)).

Imaging revealed that nanoparticles remained confined to the treated NS, with minimal diffusion across the inter-spheroid interface (figures 8(c), and S2(b)).

The ability to locally modulate one region while preserving the global circuit is a key advantage of our platform. Such compartmentalized interventions

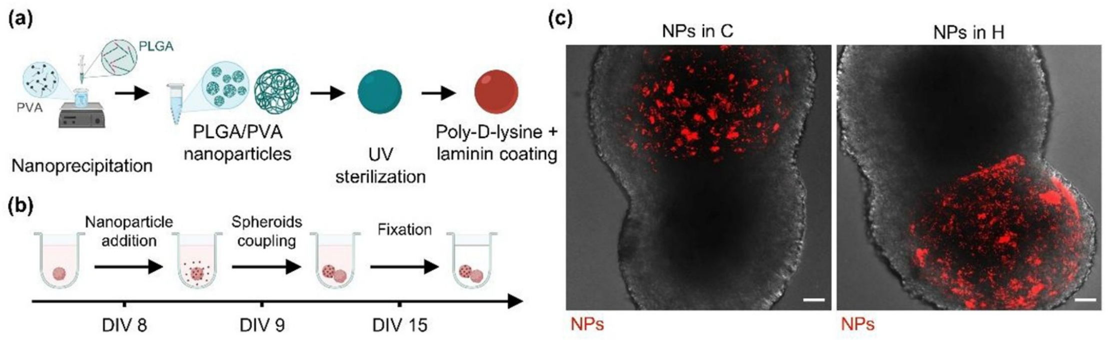

Figure 8. Fluorescent nanoparticles (NPs) in heterogeneous ASs: synthesis, deposition, and imaging. (a) Nanoparticles preparation. PLGA/PVA nanoparticles were synthesized via nanoprecipitation, sterilized under UV light for 1.5 h, and coated with a fluorescent poly-D-lysine and laminin layer. Created with BioRender.com. (b) Nanoparticles deposition on ASs. At DIV 8, nanoparticles were diluted in PBS and applied to either C or H spheroids. Created with BioRender.com. After 1 DIV, spheroids were coupled to form CH. At DIV 15, they were fixed with PFA and imaged. (c) Representative confocal images of CH with PLGA/PVA fluorescent nanoparticles localized in either the C (left) or H (right) regions. Scale bars, 50 μm.

enable the dissection of both direct and indirect effects of pharmacological agents within interconnected structures. The approach is particularly relevant for modelling diseases characterized by regionally distinct vulnerability such as Alzheimer's disease, which features both cortical and hippocampal dysfunction [60].

Our assembloid-like model provides a tractable and physiologically relevant platform for investigating brain network development *in vitro*, integrating modular architecture, functional specificity, and reproducibility within a cost-effective scaffold-free design. By bridging the simplicity and rapid maturation and high reproducibility of 2D cultures with the structural complexity of 3D organoids, it overcomes the limitations of both systems, offering a valuable compromise for both mechanistic investigations and translational or preclinical applications.

Data availability statement

The data that support the findings of this study are openly available at the following URL/DOI: https://doi.org/10.5281/zenodo.14945828 [88].

Scaffold-Free Neural Assembly available at http://doi.org/10.1088/1758-5090/ae3c42/data1.

Acknowledgments

This work was supported by #NEXTGENERATIONEU (NGEU) and funded by the Ministry of University and Research (MUR), National Recovery and Resilience Plan (NRRP), project MNESYS(PE0000006)—A Multiscale integrated approach to the study of nervous system in health and disease (DN. 1553 11.10.2022).

The authors wish to thank Dr Monica Roascio for her valuable suggestions on the fEI analysis and Professor Roberto Raiteri for the useful discussion about AFM analysis.

Author contributions

Ilaria Donati della Lunga 0009-0002-1621-8306
Data curation (equal), Formal analysis (equal), Software (equal), Visualization (equal), Writing – original draft (equal)

Francesca Callegari 0000-0002-8381-7360
Investigation (equal), Methodology (equal), Writing – original draft (equal)

Fabio Poggio 0000-0002-7354-5314
Formal analysis (equal), Software (equal), Writing – review & editing (equal)

Letizia Cerutti 0009-0008-7088-3597
Investigation (equal), Visualization (equal), Writing – original draft (equal)

Mattia Pesce
Methodology (equal), Writing – review & editing (equal)

Giovanni Lo Bello
Investigation (equal), Writing – review & editing (equal)

Alessandro Simi 0000-0002-0427-8523
Methodology (equal), Writing – review & editing (equal)

Mariateresa Tedesco
Methodology (equal), Writing – review & editing (equal)

Paolo Massobrio 0000-0001-8335-3407
Conceptualization (equal), Project administration (equal), Resources (lead), Supervision (equal), Writing – original draft (equal)

Martina Brofiga 0000-0003-2993-0597
Conceptualization (equal), Data curation (equal), Investigation (equal), Methodology (equal), Project administration (lead), Supervision (equal), Writing – original draft (equal)

References

[1] Foglietta F, Canaparo R, Muccioli G, Terreno E and Serpe L 2020 Methodological aspects and pharmacological applications of three-dimensional cancer cell cultures and organoids *Life Sci.* **254** 117784

[2] Xie R, Pal V, Yu Y, Lu X, Gao M, Liang S, Huang M, Peng W and Ozbolat I T 2024 A comprehensive review on 3D tissue models: biofabrication technologies and preclinical applications *Biomaterials* **304** 122408

[3] Callegari F, Brofiga M, Tedesco M and Massobrio P 2024 Electrophysiological features of cortical 3D networks are deeply modulated by scaffold properties *APL Bioeng.* **8** 036112

[4] Frega M, Tedesco M, Massobrio P, Pesce M and Martinoia S 2014 Network dynamics of 3D engineered neuronal cultures: a new experimental model for *in-vitro* electrophysiology *Sci. Rep.* **4** 5489

[5] Fennema E, Rivron N, Rouwkema J, van Blitterswijk C and de Boer J 2013 Spheroid culture as a tool for creating 3D complex tissues *Trends Biotechnol.* **31** 108–15

[6] Urich E, Patsch C, Aigner S, Graf M, Iacone R and Freskgård P-O 2013 Multicellular Self-assembled spheroidal model of the blood brain barrier *Sci. Rep.* **3** 1500

[7] Rabadan M A *et al* 2022 An *in vitro* model of neuronal ensembles *Nat. Commun.* **13** 1–17

[8] Dingle Y-T L, Boutin M E, Chirila A M, Livi L L, Labriola N R, Jakubek L M, Morgan J R, Darling E M, Kauer J A and Hoffman-Kim D 2015 Three-dimensional neural spheroid culture: an *in vitro* model for cortical studies *Tissue Eng. C* **21** 1274–83

[9] Mao S, Fonder C, Rubby M F, Phillips G J, Sakaguchi D S and Que L 2023 An integrated microfluidic chip for studying the effects of neurotransmitters on neurospheroids *Lab Chip* **23** 1649–63

[10] Pașca A M *et al* 2015 Functional cortical neurons and astrocytes from human pluripotent stem cells in 3D culture *Nat. Methods* **12** 671–8

[11] Amin N D and Pașca S P 2018 Building models of brain disorders with three-dimensional organoids *Neuron* **100** 389–405

[12] Miura Y, Li M-Y, Revah O, Yoon S-J, Narazaki G and Pașca S P 2022 Engineering brain assembloids to interrogate human neural circuits *Nat. Protocol.* **17** 15–35

[13] Levy R J and Pașca S P 2025 From organoids to assembloids: experimental approaches to study human neuropsychiatric disorders *Annu. Rev. Neurosci.* **48** 363–79

[14] Pașca S P *et al* 2024 A framework for neural organoids, assembloids and transplantation studies *Nature* **639** 315–20

[15] Wu S, Wang D and Liu Y 2023 Brain assembloid: a human model for neural circuits research *Life Med.* **2** lnad031

[16] Hernández D, Rooney L A, Daniszewski M, Gulluyan L, Liang H H, Cook A L, Hewitt A W and Pébay A 2022 Culture variabilities of human iPSC-derived cerebral organoids are a major issue for the modelling of phenotypes observed in Alzheimer's disease *Stem. Cell Rev. Rep.* **18** 718–31

[17] Quadrato G *et al* 2017 Cell diversity and network dynamics in photosensitive human brain organoids *Nature* **545** 48–53

[18] Kanton S *et al* 2019 Organoid single-cell genomic atlas uncovers human-specific features of brain development *Nature* **574** 418–22

[19] Aisenbrey E A and Murphy W L 2020 Synthetic alternatives to Matrigel *Nat. Rev. Mater.* **5** 539–51

[20] Bardy C *et al* 2015 Neuronal medium that supports basic synaptic functions and activity of human neurons *in vitro* *Proc. Natl Acad. Sci.* **112** E2725–34

[21] Schneider C A, Rasband W S and Eliceiri K W 2012 NIH image to ImageJ: 25 years of image analysis *Nat. Methods* **9** 671–5

[22] Kontomaris S V and Malamou A 2020 Hertz model or Oliver & Pharr analysis? Tutorial regarding AFM nanoindentation experiments on biological samples *Mater. Res. Express* **7** 033001

[23] Schindelin J *et al* 2012 Fiji: an open-source platform for biological-image analysis *Nat. Methods* **9** 676–82

[24] Montalà-Flaquer M, López-León C F, Tornero D, Houben A M, Fardet T, Monceau P, Bottani S and Soriano J 2022 Rich dynamics and functional organization on topographically designed neuronal networks *in vitro* *iScience* **25** 105680

[25] Grewe B F, Langer D, Kasper H, Kampa B M and Helmchen F 2010 High-speed *in vivo* calcium imaging reveals neuronal network activity with near-millisecond precision *Nat. Methods* **7** 399–405

[26] Kreuz T, Mulansky M and Bozanic N 2015 SPIKY: a graphical user interface for monitoring spike train synchrony *J. Neurophysiol.* **113** 3432–45

[27] Bruining H *et al* 2020 Measurement of excitation-inhibition ratio in autism spectrum disorder using critical brain dynamics *Sci. Rep.* **10** 9195

[28] Colombi I, Mahajani S, Frega M, Gasparini L and Chiappalone M 2013 Effects of antiepileptic drugs on hippocampal neurons coupled to micro-electrode arrays *Front. Neuroeng.* **6** 64279

[29] Zhuang P, Sun A X, An J, Chua C K and Chew S Y 2018 3D neural tissue models: from spheroids to bioprinting *Biomaterials* **154** 113–33

[30] Südhof T C 2021 The cell biology of synapse formation *J. Cell Biol.* **220**

[31] Gebicke-Haerter P J 2023 The computational power of the human brain *Front. Cell Neurosci.* **17** 1220030

[32] Barnes J M, Przybyla L, Weaver V M and Ewald A 2017 Tissue mechanics regulate brain development, homeostasis and disease ed A Ewald *J. Cell Sci.* **130** 71–82

[33] Budday S, Ovaert T C, Holzapfel G A, Steinmann P and Kuhl E 2020 Fifty shades of brain: a review on the mechanical testing and modeling of brain *Tissue Archives Comput. Methods Eng.* **27** 1187–230

[34] Feng H, Moakley D F, Chen S, McKenzie M G, Menon V and Zhang C 2021 Complexity and graded regulation of neuronal cell-type–specific alternative splicing revealed by single-cell RNA sequencing *Proc. Natl Acad. Sci.* **118** e2013056118

[35] Xing W, de Lima A D and Voigt T 2021 The structural E/I balance constrains the early development of cortical network activity *Front. Cell Neurosci.* **15** 687306

[36] Herculano-Houzel S 2014 The glia/neuron ratio: how it varies uniformly across brain structures and species and what that means for brain physiology and evolution *Glia* **62** 1377–91

[37] Sahara S, Yanagawa Y, O'Leary D D M and Stevens C F 2012 The fraction of cortical GABAergic neurons is constant from near the start of cortical neurogenesis to adulthood *J. Neurosci.* **32** 4755–61

[38] Prestigio C, Ferrante D, Valente P, Casagrande S, Albanesi E, Yanagawa Y, Benfenati F and Baldelli P 2019 Spike-related electrophysiological identification of cultured hippocampal excitatory and inhibitory neurons *Mol. Neurobiol.* **56** 6276–92

[39] van Groen T, Miettinen P and Kadish I 2003 The entorhinal cortex of the mouse: organization of the projection to the hippocampal formation *Hippocampus* **13** 133–49

[40] Kemppainen S, Jolkkonen E and Pitkänen A 2002 Projections from the posterior cortical nucleus of the amygdala to the hippocampal formation and parahippocampal region in rat *Hippocampus* **12** 735–55

[41] Tibau E, Valencia M and Soriano J 2013 Identification of neuronal network properties from the spectral analysis of calcium imaging signals in neuronal cultures *Front. Neural Circuits* **7** 72027

[42] Soriano J, Martínez M R, Tlusty T and Moses E 2008 Development of input connections in neural cultures *Proc. Natl Acad. Sci. USA* **105** 13758–63

[43] Ganguly K, Schinder A F, Wong S T and Poo M-M 2001 GABA itself promotes the developmental switch of neuronal GABAergic responses from excitation to inhibition *Cell* **105** 521–32

[44] Jorfi M, D'Avanzo C, Kim D Y and Irimia D 2018 Three-dimensional models of the human brain development and diseases *Adv. Healthcare Mater.* **7** 1700723

[45] Cerutti L and Brofiga M 2024 Unraveling brain diseases: the promise of brain-on-a-chip models *J. Neurosci. Methods* **405** 110105

[46] Brofiga M, Callegari F, Cerutti L, Tedesco M and Massobrio P 2025 Cortical, striatal, and thalamic populations self-organize into a functionally connected circuit with long-term memory properties *Biosens. Bioelectron.* **267** 116840

[47] Dauth S, Maoz B M, Sheehy S P, Hemphill M A, Murty T, Macedonia M K, Greer A M, Budnik B and Parker K K 2017 Neurons derived from different brain regions are inherently different *in vitro*: a novel multiregional brain-on-a-chip *J. Neurophysiol.* **117** 1320–41

[48] Deleglise B *et al* 2013 Synapto-protective drugs evaluation in reconstructed neuronal network ed G J Guillemin *PLoS One* **8** e71103

[49] Cadamuro F, Nicotra F and Russo L 2023 3D printed tissue models: from hydrogels to biomedical applications *J. Control Release* **354** 726–45

[50] Huang W-H, Ding S-L, Zhao X-Y, Li K, Guo H-T, Zhang M-Z and Gu Q 2023 Collagen for neural tissue engineering: materials, strategies, and challenges *Mater. Today Bio* **20** 100639

[51] Mateus J C, Sousa M M, Burrone J and Aguiar P 2024 Beyond a transmission cable—new technologies to reveal the richness in axonal electrophysiology *J. Neurosci.* **44** e1446232023

[52] Osaki T, Duenki T, Chow S Y A, Ikegami Y, Beaubois R, Levi T, Nakagawa-Tamagawa N, Hirano Y and Ikeuchi Y 2024 Complex activity and short-term plasticity of human cerebral organoids reciprocally connected with axons *Nat. Commun.* **15** 1–13

[53] Skardal A 2024 Grand challenges in organoid and organ-on-a-chip technologies *Front. Bioeng. Biotechnol.* **12** 1366280

[54] Yin X, Mead B E, Safaee H, Langer R, Karp J M and Levy O 2016 Engineering stem cell organoids *Cell Stem Cell* **18** 25–38

[55] Kim Y-G and Lee Y-I 2012 Differential expressions of synaptogenic markers between primary cultured cortical and hippocampal neurons *Exp. Neurobiol.* **21** 61–67

[56] Koser D E *et al* 2016 Mechanosensing is critical for axon growth in the developing brain *Nat. Neurosci.* **19** 1592–8

[57] Perez J E, Jan A, Villard C and Wilhelm C 2023 Surface tension and neuronal sorting in magnetically engineered brain-like tissue *Adv. Sci.* **10** 2302411

[58] Bernardinelli Y, Muller D and Nikonenko I 2014 Astrocyte-synapse structural plasticity *Neural Plast.* **2014** 1–13

[59] Bélanger M, Allaman I and Magistretti P J 2011 Brain energy metabolism: focus on astrocyte-neuron metabolic cooperation *Cell Metab.* **14** 724–38

[60] Brofiga M, Pisano M, Tedesco M, Boccaccio A and Massobrio P 2022 Functional inhibitory connections modulate the electrophysiological activity patterns of cortical-hippocampal ensembles *Cereb. Cortex* **32** 1866–81

[61] Panzeri S, Macke J H, Gross J and Kayser C 2015 Neural population coding: combining insights from microscopic and mass signals *Trends Cognit. Sci.* **19** 162–72

[62] DeBello W M, McBride T J, Nichols G S, Pannoni K E, Sanculi D and Totten D J 2014 Input clustering and the microscale structure of local circuits *Front. Neural Circuits* **8** 77675

[63] İpek Ö, Abbas F, Sajidy H and Canepari M 2025 Fast neuronal calcium signals in brain slices loaded with Fluo-4 AM Ester *Eur. J. Neurosci.* **61** e16657

[64] Orlandi J G, Soriano J, Alvarez-Lacalle E, Teller S and Casademunt J 2013 Noise focusing and the emergence of coherent activity in neuronal cultures *Nat. Phys.* **9** 582–90

[65] Teller S, Granell C, De Domenico M, Soriano J, Gómez S, Arenas A and Gutkin B S 2014 Emergence of assortative mixing between clusters of cultured neurons *PLoS Comput. Biol.* **10** e1003796

[66] Stetter O, Battaglia D, Soriano J, Geisel T and Beggs J 2012 Model-free reconstruction of excitatory neuronal connectivity from calcium imaging signals *PLoS Comput. Biol.* **8** e1002653

[67] Tibau E, Ludl A-A, Rudiger S, Orlandi J G and Soriano J 2020 Neuronal spatial arrangement shapes effective connectivity traits of *in vitro* cortical networks *IEEE Trans. Netw. Sci. Eng.* **7** 435–48

[68] Jeong S *et al* 2023 Integration of reconfigurable microchannels into aligned three-dimensional neural networks for spatially controllable neuromodulation *Sci. Adv.* **9** eadf0925

[69] Teller S, Tahirbegi I B, Mir M, Samitier J and Soriano J 2015 Magnetite-Amyloid-β deteriorates activity and functional organization in an *in vitro* model for Alzheimer's disease *Sci. Rep.* **5** 1–16

[70] Hughes S 2011 Thalamic gap junctions control local neuronal synchrony and influence macroscopic oscillation amplitude during EEG alpha rhythms *Front. Psychol.* **2** 10734

[71] Aminoff M J 2012 *Electroencephalography Aminoff's Electrodiagnosis in Clinical Neurology* (Elsevier) pp 37–84

[72] López-Madrona V J, Pérez-Montoyo E, Álvarez-Salvado E, Moratal D, Herreras O, Pereda E, Mirasso C R and Canals S 2020 Different theta frameworks coexist in the rat hippocampus and are coordinated during memory-guided and novelty tasks *Elife* **9** 1–35

[73] Colgin L L and Moser E I 2010 Gamma oscillations in the hippocampus *Physiology* **25** 319–29

[74] Daume J, Gruber T, Engel A K and Friese U 2017 Phase-amplitude coupling and long-range phase synchronization reveal frontotemporal interactions during visual working memory *J. Neurosci.* **37** 313–22

[75] Kopell N, Ermentrout G B, Whittington M A and Traub R D 2000 Gamma rhythms and beta rhythms have different synchronization properties *Proc. Natl Acad. Sci.* **97** 1867–72

[76] Buzsáki G and Wang X-J 2012 Mechanisms of gamma oscillations *Annu. Rev. Neurosci.* **35** 203–25

[77] Nyhus E and Curran T 2010 Functional role of gamma and theta oscillations in episodic memory *Neurosci. Biobehav. Rev.* **34** 1023–35

[78] Fries P, Nikolić D and Singer W 2007 The gamma cycle *Trends Neurosci.* **30** 309–16

[79] Uhlhaas P J, Roux F, Rodriguez E, Rotarska-Jagiela A and Singer W 2010 Neural synchrony and the development of cortical networks *Trends Cognit. Sci.* **14** 72–80

[80] Shein Idelson M, Ben-Jacob E, Hanein Y and Sporns O 2010 Innate synchronous oscillations in freely-organized small neuronal circuits *PLoS One* **5** e14443

[81] Sharf T *et al* 2022 Functional neuronal circuitry and oscillatory dynamics in human brain organoids *Nat. Commun.* **13** 1–20

[82] Fitzgerald M Q, Chu T, Puppo F, Blanch R, Chillón M, Subramaniam S and Muotri A R 2024 Generation of 'semi-guided' cortical organoids with complex neural oscillations *Nat. Protocol.* **19** 2712–38

[83] Pachitariu M, Lyamzin D R, Sahani M and Lesica N A 2015 State-dependent population coding in primary auditory cortex *J. Neurosci.* **35** 2058–73

[84] Urbain N, Fourcaud-Trocmé N, Laheux S, Salin P A and Gentet L J 2019 Brain-state-dependent modulation of neuronal firing and membrane potential dynamics in the somatosensory thalamus during natural sleep *Cell Rep.* **26** 1443–1457.e5

[85] Bonansco C and Fuenzalida M 2016 Plasticity of hippocampal excitatory-inhibitory balance: missing the synaptic control in the epileptic brain *Neural Plast.* **2016** 1–13

[86] Huang W and Zhang C 2018 Tuning the size of poly(lactic-co-glycolic Acid) (PLGA) nanoparticles fabricated by nano-precipitation *Biotechnol. J.* **13** 1700203

[87] Kam L 2001 Axonal outgrowth of hippocampal neurons on micro-scale networks of polylysine-conjugated laminin *Biomaterials* **22** 1049–54

[88] Brofiga M 2025 CxHp_Neurospheroids (https://doi.org/10.5281/zenodo.14945828)